INTERNATIONAL JOURNAL FOR NUMERICAL METHODS IN FLUIDS
Int. J. Numer. Meth. Fluids (2014)
Published online in Wiley Online Library (wileyonlinelibrary.com). DOI: 10.1002/fld.3936

RESEARCH PAPER PRESENTED AT THE 8TH SYMPOSIUM ON NUMERICAL ANALYSIS OF FLUID FLOW AND HEAT TRANSFER 2013

Application of a thermodynamically compatible two-phase flow model to the high-resolution simulations of compressible gas–magma flow

D. Zeidan[1,*,†], R. Touma[2] and A. Slaouti[3]

[1]*School of Natural Resources Engineering and Management, German Jordanian University, Amman, Jordan*
[2]*Department of Computer Science & Mathematics, Lebanese American University, Beirut, Lebanon*
[3]*School of Engineering and Technology, PSB Academy, Singapore*

SUMMARY

This paper reports on the application and development of a fully hyperbolic and fully conservative two-phase flow model for the simulation of gas and magma flow within volcanic processes. The model solves a set of mixture conservation equations for the gas and magma two-phase flow with velocity non-equilibrium. In this model, the effect of the relative velocity is introduced by a kinetic constitutive equation with other equations for volume and mass fractions of the gas phase. The model is examined numerically by the widely used finite volume Godunov methods of centered-type. Using the Riemann problem, we numerically simulate wave propagation and the development of shocks and rarefactions in volcanic eruptions. These simulations are of magma fragmentation type where the relative velocity continues to dominate. A series of test cases whose solution contains features relevant to gas–magma mixtures are conducted. In particular, numerical results indicate that the model implementation predicts key features of the relative velocity within volcanic processes without any mathematical or physical simplifications. Simulation results are sharply and accurately provided without any spurious oscillations in all of the flow variables. The numerical methods and results are also compared with other numerical methods available in the literature. It is found that the provided resolutions are more accurate for the considered test cases. Copyright © 2014 John Wiley & Sons, Ltd.

Received 31 January 2014; Revised 12 May 2014; Accepted 12 June 2014

KEY WORDS: two-phase flows; volcanic eruption; fragmented magma; velocity non-equilibrium; TVD SLIC scheme; numerical simulation

1. INTRODUCTION

Although mathematical and numerical models describing gas–solid and gas–liquid two-phase flows with applications to industrial processes have been investigated in detail, there are fewer studies dedicated to volcanic eruptions (see, for example, [1–3]). These studies can be put into two groups, namely, two-fluid models and diffusion models [4, 5]. Although these models have been used by many researchers, they cannot be applied to non-equilibrium phenomena. A fundamental issue in all these studies for two-phase flows is the hyperbolicity and conservativity of such models. In many of these models, hyperbolicity can be generated under certain restrictions but non-conservative terms are inherited in their final formulations. To overcome such problems, another class of models have been proposed and applied to different two-phase flow problems (see, for example, [6–10] and the

*Correspondence to: D. Zeidan, School of Natural Resources Engineering and Management, German Jordanian University, Amman, Jordan.
†E-mail: dia.zeidan@gju.edu.jo; diazeidan@yahoo.com; diazeidan@gmail.com

references therein). This class of mathematical models is based on the theory of thermodynamically compatible systems of hyperbolic conservation laws [11]. The model is fully conservative, fully hyperbolic, and independent of the type of numerical method used to employ it.

In the present work, we intend to take the advantages of the fully conservative and fully hyperbolic mathematical model proposed in the literature to investigate two-phase flows arising within volcanic eruptions phenomena. Such flows are characterized by the large differences in the thermodynamical, chemical, and physical nature of the two phases. These flows are, in general, unsteady multiphase flow phenomena forming different volcanic systems such as eruption and conduit column processes [12–14]. The flow within such systems is associated with magma chemical and physical compositions that form different magma fragments. Depending on magma fragmentation, the flow may behave as bubbly magma at high viscosity, that is, magma before fragmentation or a mixture of volcanic gas and pyroclasts (hot ash) with very low viscosity, that is, after fragmentation, which is the interest of the current paper. A large amount of literature has been published for such processes, see, for example, [15–18]. Most of these studies describe two-phase flows during volcanic eruptions involving a steady-state approach. In recent years, these studies have been further developed to unsteady approaches of specific interest. For instance, an incompressible single-phase model was presented in [19] that is based on empirical relations of [20]. A theoretical steady model was developed in [21, 22] on the basis of shock tube theory to investigate the connection between magma properties and explosive eruptions dynamics. In [23], another single-phase model was presented that accounts for the energy conservation expression but does not account for compressible flows. A model was presented in [24] to solve separately a set of Navier–Stokes equations for compressible gas and incompressible solid phases within Plinian eruption. Another model was also presented in [25, 26] on the basis of microscopic particle dynamics simulations to explore non-equilibrium behavior of volcanoes. In [27, 28], an isothermal model was developed to investigate magma ascent in volcanic eruptions. Although these are some remarkable studies in understanding the volcanic two-phase flow processes, they are limited to mechanical, thermal, and velocity equilibrium. Even with mechanical and thermal non-equilibrium being taken into account with such studies, phase velocities are always considered to be in equilibrium. The inclusion of the interphase drag source term in the momentum equations takes into account the relative velocity between the two phases. Within this state of affairs lie significant interests in this relative velocity aspect that possess many desirable characteristics for volcanic eruptions phenomena.

The main objective of the present work is to study a mixture of volcanic gas and magma fragmentations with velocity non-equilibrium. This relative velocity is represented by a kinetic constitutive equation that can be attributed to the work of the drag force. Further, we will adopt a model developed previously in [29], which is imported into the mixture model to study wave propagation within volcanic two-phase flows. Using such a model would lead to greatly improved coupling between the dynamics of explosive eruptions magma properties. With this coupling, the present work will contribute to establishing a framework for understanding the relative velocity analysis encountered in volcanic eruptions. As mentioned earlier, this model is inherently hyperbolic and conservative as an initial boundary value problem for gas–magma mixtures. These are highly desirable features from a numerical point of view as one can apply any numerical approach of interest. Further, with such features, the current mixture model relieves the application of single-phase flow numerical methods. In this paper, we intend to take the advantage of the slope limiter centered (SLIC) scheme for the numerical simulation of the present model. The SLIC scheme is a Godunov method of centered-type and was originally proposed in [30] for Euler equations and has been successful in applications for single-phase and two-phase flows (see, for example, [29, 31] and the references therein). We chose the Godunov method of centered-type due to the large number of governing equations that lead to the large number of waves. In this respect, obtaining an analytical solution and employing upwind methods in producing accurate resolutions to the Riemann problem become a very challenging task. The SLIC scheme thus significantly solves the Riemann problem numerically, although centered methods are more dissipative than the upwind methods, simple and have the lowest numerical viscosity between centered methods. The SLIC scheme is well-documented in the literature for which we refer the reader to [32] for further details.

DOI: 10.1002/fld

In Section 2, we give a brief description of the model equations proposed in [29], which have been applied to gas and magma mixtures of the current investigation. The numerical methods that take advantage of the mathematical features of the model equations are described in Section 3. The SLIC scheme is given in this section. Numerical results produced by Godunov methods are presented and compared in Section 4. These results show how both the model and methods deal with volcanic processes accurately and sufficiently. The paper ends with concluding remarks summarizing our finding and presents an outlook for future work.

2. MIXTURE MODEL

As mentioned in the introduction, the currently used mathematical models describing gas–magma two-phase flows of volcanic eruptions are inherently non-hyperbolic and formulated in non-conservative form. This paper focuses precisely on a fully hyperbolic two-phase flow model in a conservative form originally presented in [29]. The mathematical description is based in terms of parameters of state for the mixture model of two-phase flows in which the influence of the relative velocity is fully taken into account. The specific application of such model to volcanic gas and fragment magma mixtures is presented here and specified by two sets of PDE. A set represents the mixture mass, mixture momentum, and mixture energy; and another set represents the volume fraction and mass fraction for the gas phase and the relative velocity between the gas and magma phases. These can be written in the following conservative form:

- Balance laws for the mixture.

$$\frac{\partial}{\partial t}(\rho) + \frac{\partial}{\partial x}(\rho u) = 0, \tag{1}$$

$$\frac{\partial}{\partial t}(\rho u) + \frac{\partial}{\partial x}\left(\rho u^2 + P + \rho c(1-c)u_r^2\right) = 0, \tag{2}$$

$$\frac{\partial}{\partial t}(\rho E) + \frac{\partial}{\partial x}\left(\rho u E + P u + \rho c(1-c)u_r\left(u u_r + (1-2c)\frac{u_r^2}{2} + \frac{\partial e}{\partial c}\right)\right) = 0. \tag{3}$$

- Volume and mass fractions for the gas phase and the relative velocity between the gas and magma phases.

$$\frac{\partial}{\partial t}(\rho\alpha) + \frac{\partial}{\partial x}(\rho u\alpha) = 0, \tag{4}$$

$$\frac{\partial}{\partial t}(\rho c) + \frac{\partial}{\partial x}(\rho u c + \rho c(1-c)u_r) = 0, \tag{5}$$

$$\frac{\partial}{\partial t}(u_r) + \frac{\partial}{\partial x}\left(u u_r + (1-2c)\frac{u_r^2}{2} + e_c\right) = \pi. \tag{6}$$

It is assumed that gas exsolution is negligible, that is, no mass transfer between the phases and no viscous effects in both phases. The aforementioned sets of conservation equations include both mixture and phase flow variables. We define the following terms as follows:

- The gas mass void fraction: $c_2 = \alpha_2\rho_2\rho^{-1} = c$,
- The mixture velocity: $u = c_2u_2 + c_1u_1$,
- The relative velocity between the two phases: $u_r = u_2 - u_1$,
- The mixture density: $\rho = \alpha_2\rho_2 + \alpha_1\rho_1 = \alpha\rho_2 + (1-\alpha)\rho_1$,

where the subscripts refer to the magma, 1, and gas, 2, phases, respectively. The volume fractions satisfy the relation

DOI: 10.1002/fld

$$\alpha_2 + \alpha_1 = 1, \tag{7}$$

and the mixture total energy is defined in terms of the mixture internal energy

$$E = e\left(P, \alpha, c, \rho\right) + \frac{u^2}{2} + c(1-c)\frac{u_r^2}{2}, \tag{8}$$

where the mixture internal energy is defined as

$$e = c_2 e_2\left(P_2, \rho_2\right) + c_1 e_1\left(P_1, \rho_1\right), \tag{9}$$

which requires equations of state suitable for pure gas and pure magma. Further, each phase possesses its own pressure that is calculated using the following relations

$$P_2 = \rho_2^2 \frac{\partial e_2}{\partial \rho_2} \quad \text{and} \quad P_1 = \rho_1^2 \frac{\partial e_1}{\partial \rho_1}. \tag{10}$$

With the help of the aforementioned relations, the mixture pressure is determined as

$$P = \alpha_2 P_2 + \alpha_1 P_1. \tag{11}$$

The term on the right-hand side of Equation 6 represents the effect of interphase drag force combined in π. This drag force is commonly expressed in the following constitutive relation

$$\pi = \kappa(u_2 - u_1) = \kappa u_r, \tag{12}$$

where the coefficient κ is the drag function. While studies on currently used volcanic two-phase flow models show the presence of such force in a precise manner within the momentum balance laws, the current model provides another means of exploring the importance of the drag force through Equation 6. The different forms of the interphase drag force in various flow processes have been discussed extensively in the literature (see for instance [33–37] for such forms and applications).

In the framework of conservativity formulation, the aforementioned system is fully conservative in terms of mixture and phase parameters of state. A detailed development and presentation of the eigenstructure of the current model is exposed in [29]. Theoretical justification and observations to the characteristic analysis of such a model have resulted in salient features that form the basic wave structure of the solution of the Riemann problem for practical problems such as explosive eruptions.

3. NUMERICAL APPROACH TO SOLVE THE MODEL EQUATIONS

The hyperbolic conservation equations for the one-dimensional gas and magma mixture can be written as

$$\frac{\partial \mathbb{U}}{\partial t} + \frac{\partial \mathbb{F}(\mathbb{U})}{\partial x} = \mathbb{S}(\mathbb{U}), \quad t > 0, \quad -\infty < x < \infty. \tag{13}$$

Here, $\mathbb{U}$ is the vector of conservative variables and $\mathbb{F}(\mathbb{U})$ is the numerical flux vector which, respectively, corresponds to

$$\mathbb{U} = \begin{pmatrix} \rho \\ \rho\alpha \\ \rho u \\ \rho c \\ u_r \\ \rho E \end{pmatrix} \text{and} \quad \mathbb{F}(\mathbb{U}) = \begin{pmatrix} \rho u \\ \rho u \alpha \\ \rho u^2 + P + \rho u_r E_{u_r} \\ \rho u c + \rho E_{u_r} \\ u u_r + E_c \\ \rho u E + P u + \rho u u_r E_{u_r} + \rho E_c E_{u_r} \end{pmatrix}, \tag{14}$$

where the notations E_c and E_{u_r} appearing in the expression of the fluxes can be found from the total energy (8). Further, the source terms can be written as

$$\mathbb{S}(\mathbb{U}) = [0, 0, 0, 0, \pi, 0]^T. \tag{15}$$

DOI: 10.1002/fld

The problem of solving (13) with constant initial condition is known as the Riemann problem that can be solved either exactly, analytically, or numerically. However, solving (13) analytically fully is not possible because of the large number of different waves involved in the Riemann problem. Shortage of such analytical solution for such equations motivates the recourses to numerical solution techniques.

The model formulated in (13) can be solved by any numerical method of interest. In this respect, one would aim for accurate and efficient numerical solutions. Thus, the concept of finite volume Godunov-centered methods to calculate the numerical solution is used. Based on finite volume formulations then, a computational cell volume $\left[x_{i-\frac{1}{2}}, x_{i+\frac{1}{2}}\right]\times\left[t^n, t^{n+1}\right]$ with cell boundaries defined as $x_{i\pm\frac{1}{2}}$, cell spacing, and time step are given by $\Delta x = x_{i+\frac{1}{2}} - x_{i-\frac{1}{2}}$ and $\Delta t = t^{n+1} - t^n$, where $i = 1, \ldots, N$, N is the number of cells, and n is the number of time steps leads to the following homogeneous discretization formula

$$\mathbb{U}_i^{n+1} = \mathbb{U}_i^n - \frac{\Delta t}{\Delta x}\left[\mathbb{F}^n_{i+\frac{1}{2}} - \mathbb{F}^n_{i-\frac{1}{2}}\right]. \tag{16}$$

In (16), the source terms $\mathbb{S}(\mathbb{U})$ are excluded from the computational analysis, $\mathbb{U}_i^n$ and $\mathbb{F}^n_{i\pm\frac{1}{2}}$ are the numerical approximation of cell averaged for the vector of conserved variables and the numerical flux functions as in (14), respectively. These fluxes can be calculated by solving the initial boundary value problem of system (13) in process without dissipation together with the following initial data

$$\mathbb{U}(x, t^n) = \begin{cases} \mathbb{U}_L & x < x_{i+\frac{1}{2}}, \\ \mathbb{U}_R & x > x_{i+\frac{1}{2}}, \end{cases} \tag{17}$$

where $\mathbb{U}_L$ and $\mathbb{U}_R$ are discontinuous left and right constant states on either side of the interface which is known as the Godunov approach for solving the Riemann problem of system (13). Within the framework of Godunov methods of centered-type, the numerical fluxes can be approximated by solving the local Riemann problem numerically using the following first-order centered (FORCE) scheme

$$\mathbb{F}^{\mathrm{FORCE}}_{i+\frac{1}{2}} = \frac{1}{2}\left(\mathbb{F}^{\mathrm{LF}}_{i+\frac{1}{2}} + \mathbb{F}^{\mathrm{RI}}_{i+\frac{1}{2}}\right). \tag{18}$$

Here, $\mathbb{F}^{\mathrm{LF}}_{i+\frac{1}{2}}$ is the Lax–Friedrichs flux given by

$$\mathbb{F}^{\mathrm{LF}}_{i+\frac{1}{2}} = \frac{1}{2}\left[\mathbb{F}(\mathbb{U}_i^n) + \mathbb{F}(\mathbb{U}_{i+1}^n)\right] + \frac{1}{2}\frac{\Delta x}{\Delta t}\left[\mathbb{U}_i^n - \mathbb{U}_{i+1}^n\right], \tag{19}$$

and the following describes the Richtmyer flux

$$\mathbb{F}^{\mathrm{RI}}_{i+\frac{1}{2}} = \mathbb{F}(\mathbb{U}_{i+\frac{1}{2}}), \quad \mathbb{U}^{\mathrm{RI}}_{i+\frac{1}{2}} = \frac{1}{2}\left(\mathbb{U}_i^n + \mathbb{U}_{i+1}^n\right) + \frac{1}{2}\frac{\Delta t}{\Delta x}\left[\mathbb{F}(\mathbb{U}_i^n) - \mathbb{F}(\mathbb{U}_{i+1}^n)\right]. \tag{20}$$

Together with monotonic upstream-centered scheme for conservation laws (MUSCL)–Hancock scheme, the FORCE flux can produce a second-order centered scheme, namely, the SLIC scheme. The SLIC scheme was developed first in [30] and then adapted to two-phase flows in [29]. The SLIC scheme consists of the following three steps:

1. Data reconstruction and boundary extrapolated values. The values $\mathbb{U}_i^n$ within this step are locally restored through a piecewise linear function as

$$\mathbb{U}_i(x) = \mathbb{U}_i^n(x) + \frac{(x - x_i)}{\Delta x}\Delta_i, \tag{21}$$

which consists of changing $\mathbb{U}_i^n$ values into the following form

$$\mathbb{U}_i^L = \mathbb{U}_i^n - \frac{\Delta_i}{2} \quad \text{and} \quad \mathbb{U}_i^R = \mathbb{U}_i^n + \frac{\Delta_i}{2}. \tag{22}$$

Here, Δ_i is a limited slope vector of six components for system (13). This is employed to control spurious oscillations near strong gradients of the numerical resolution and obtained

DOI: 10.1002/fld

using total variation diminishing (TVD) constraints among various limiters. We refer to [32] for a detailed presentation of such limiters.

2. Evolution of the boundary extrapolated values. The boundary values in this step are evolved by a time $\frac{\Delta t}{2}$. This is defined as

$$\left(\mathbb{U}_i^L\right)^{\text{New}} = \mathbb{U}_i^L + \frac{1}{2}\frac{\Delta t}{\Delta x}\left[\mathbb{F}\left(\mathbb{U}_i^L\right) - \mathbb{F}\left(\mathbb{U}_i^R\right)\right], \tag{23}$$

$$\left(\mathbb{U}_i^R\right)^{\text{New}} = \mathbb{U}_i^R + \frac{1}{2}\frac{\Delta t}{\Delta x}\left[\mathbb{F}\left(\mathbb{U}_i^L\right) - \mathbb{F}\left(\mathbb{U}_i^R\right)\right], \tag{24}$$

which is a middle step that consists of two different fluxes at every intercell position $i + \frac{1}{2}$ where the intercell flux $\mathbb{F}_{i+\frac{1}{2}}$ is still has to be calculated.

3. The Riemann problem. This step is to advance the solution in time on every cell by solving the Riemann problem numerically using the following FORCE flux

$$\mathbb{F}_{i+\frac{1}{2}} = \mathbb{F}_{i+\frac{1}{2}}\left(\left(\mathbb{U}_i^R\right)^{\text{New}}, \left(\mathbb{U}_{i+1}^L\right)^{\text{New}}\right), \tag{25}$$

as given by (18) on every cell.

Having solved the Riemann problem locally, the numerical fluxes are then used to exchange information between the complete wave structure during the solution process.

4. TEST PROBLEMS AND VALIDATIONS

The major challenge in the simulation of volcanic flows is the model equations input of initial conditions related to different phases. Such values are highly influential in both geophysical and mathematical forms of volcanic processes. The simulations we choose to conduct, therefore, correspond to a realistic situation of such processes and are adequate for the purpose of this paper. Furthermore, to validate the proposed model equations, we present simulation results obtained with the method described in the previous section. This will test the ability of both the model equations and the accuracy and efficiency of the TVD SLIC scheme with problems whose physical solutions have features that are significant to volcanic process. Thus, the following standard test cases with an interface are considered in this paper: gas–magma mixture expansion tube, mixture shock tube problem, gas–magma mixture collision, and influence of the drag force. In the course of this work, the equations of state for gas proposed by a perfect gas and stiffened for magma are written as follows

$$e_2(P_2, \rho_2) = \frac{A_2}{\gamma_2 - 1}{\rho_2}^{\gamma_2 - 1}\exp\left(c\,\frac{s_2}{c_V^2}\right), \tag{26}$$

$$e_1(P_1, \rho_1) = \frac{A_1}{\gamma_1 - 1}\rho_1^{\gamma_1 - 1}\exp\left((1-c)\,\frac{s_1}{c_V^1}\right) + \frac{A_0}{\rho_1}. \tag{27}$$

Although the parameters $\gamma_2,\ c_V^2,\ A_2$ and $\gamma_1,\ c_V^1,\ A_0$, and A_1 are adjusted from experiments, we will take the following for computing purposes [38, 39]

$$\begin{aligned} &\gamma_2 = 1.43, \quad c_V^2 = 1039.86 \quad \text{and} \quad A_2 = 8.0, \\ &\gamma_1 = 2.35, \quad c_V^1 = 1815.0 \quad A_0 = 1 \times 10^5\ Pa \quad \text{and} \quad A_2 = 1.0. \end{aligned} \tag{28}$$

In all test cases, the same computational domain of the x-space is used, $[-10, 10]$, as the initial conditions will be given in each test case and Δt is determined by

$$\Delta t = \text{CFL}\frac{\Delta x}{\lambda_{\max}} \tag{29}$$

at each time step, and $\lambda_{\max}$ is the maximum wave speed of systems (1)–(6). Because no analytical solutions are available for system (13), we obtain reference solutions for all test cases by calculating

DOI: 10.1002/fld

high resolutions on 6000 using the SLIC scheme. Although an analytical solution was reported in [40] for simplified cases with certain assumptions, numerical reference solutions are still needed for the current paper. In the numerical process, we use SUPERBEE limiter within the SLIC scheme along with transmissive boundary conditions at $x = -10$ and $x = 10$ and with a CFL stability coefficient of 0.9. Finally, the performance and validation of both the TVD SLIC scheme and the provided simulation results are evaluated by comparing them to numerical methods that do not depend on the structure of the Riemann problem. We choose the commonly used numerical method, namely, the Lax–Friedrichs scheme, which is an explicit scheme and very simple to implement, the Lax–Wendroff scheme, and the recent unstaggered central scheme (UCS) of [41].

4.1. Gas–magma mixture expansion tube

We start our test cases by simulating expansion tube problem for a mixture of gas and magma. In this problem, the following initial data for the Riemann problem are considered

- Magma

$$(\rho_1, u_1, s_1)_L = \left(3800.0\ \text{kg/m}^3,\ -700.0\ \text{m/s},\ 7556.5895\ \text{J/K kg}\right),$$
$$(\rho_1, u_1, s_1)_R = \left(3800.0\ \text{kg/m}^3,\ \ 700.0\ \text{m/s},\ 7556.5895\ \text{J/K kg}\right).$$

- Gas

$$(\alpha, \rho_2, u_2, s_2)_L = \left(0.75, 1562.0\ \text{kg/m}^3,\ -700.0\ \text{m/s},\ 12658.879\ \text{J/K kg}\right),$$
$$(\alpha, \rho_2, u_2, s_2)_R = \left(0.75, 1562.0\ \text{kg/m}^3,\ \ 700.0\ \text{m/s},\ 12658.879\ \text{J/K kg}\right),$$

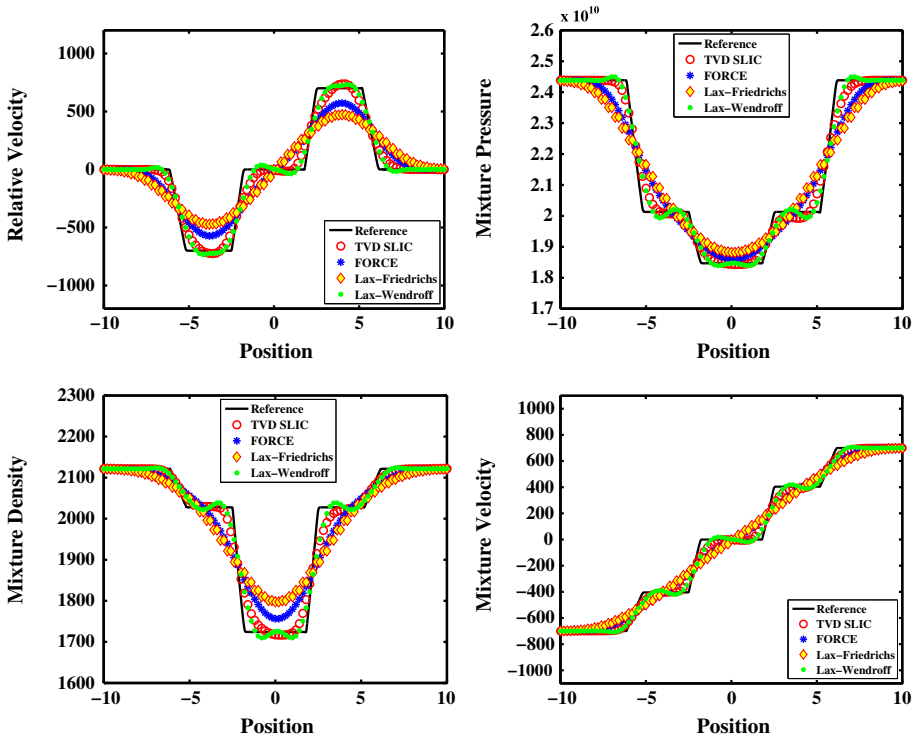

Figure 1. Results for the gas–magma mixture expansion tube (test case 4.4) at $t = 0.0008$ with a CFL of 0.9. The computed results are the symbols provided by four numerical methods on a mesh with of 100 cells. SUPERBEE limiter employed within the SLIC scheme. The solid line indicates the reference solutions provided on a very fine mesh of 6000 cells. From top to bottom and left to right: relative velocity (m s^{-1}), mixture pressure (Pa), mixture density (kg m^{-3}), and mixture velocity (m s^{-1}).

DOI: 10.1002/fld

at time $t = 0.0008$. The reference solution for such severe test case produces left and right rarefaction waves as displayed in Figure 1. Because of the nature of the solutions, the wave structure shows two left and two right rarefaction waves propagating in opposite direction separated by a repeated contact discontinuity. These left and right rarefaction waves are associated with the genuinely nonlinear field $\lambda_{1,2}$ and $\lambda_{5,6}$, respectively. The resulted wave structure appearing in Figure 1 is due to the high initial volume fraction of the gas phase and to the fact that the magma is considered as fragmented magma with high gas and magma velocities. In such case, the flow mixture takes the form of gas particle. Figure 1 shows the numerical results (symbols) obtained with the Lax–Wendroff, Lax–Friedrichs, FORCE, and TVD SLIC methods, at time $t = 0.0008$, on a coarse mesh of 100 cells. It is easy to see that these numerical results (symbols) capture the reference solution quite well. Comparing the four methods, we also note that the TVD SLIC scheme produces better results than the lower-order methods and the Lax–Wendroff scheme. Further, the head and tail of the left and right rarefaction waves are accurately reproduced as sharp features. Clearly, the results of Figure 1 demonstrate the known property of Lax–Friedrichs scheme of pairing cell values. Further, the Lax–Wendroff scheme has produced overshoots and undershoots across the middle wave and before and after the rarefaction waves.

In Figure 2, we present three different meshes: coarse, medium, and fine meshes produced to facilitate mesh convergence solutions. These computations (symbols) have been carried out to assess the accuracy and ability of the predictions for such initial data for the current Riemann problem. As one can note in this figure, the mesh convergence, obtained using the TVD SLIC scheme, approaches to the reference solution (solid lines) and in a good agreement and satisfactory in all the plots and oscillation-free. The reference solutions are produced using the TVD SLIC scheme on a very fine mesh of 6000 cells.

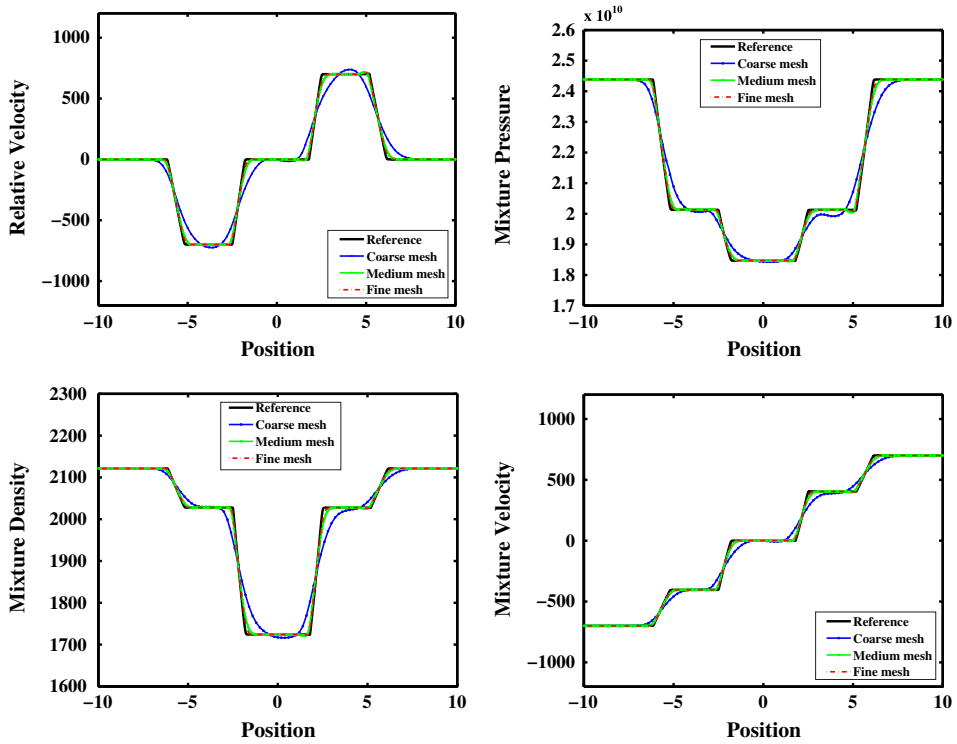

Figure 2. Mesh convergence study for the TVD SLIC scheme. The results for gas–magma mixture expansion tube test case 4.4 are computed on coarse, medium, and fine meshes at time $t = 0.0008$. It can be observed from these plots that the fine mesh has approached the reference solutions. From top to bottom and left to right: relative velocity (m s^{-1}) and mixture pressure (Pa), mixture density (kg m^{-3}) and mixture velocity (m s^{-1}).

DOI: 10.1002/fld

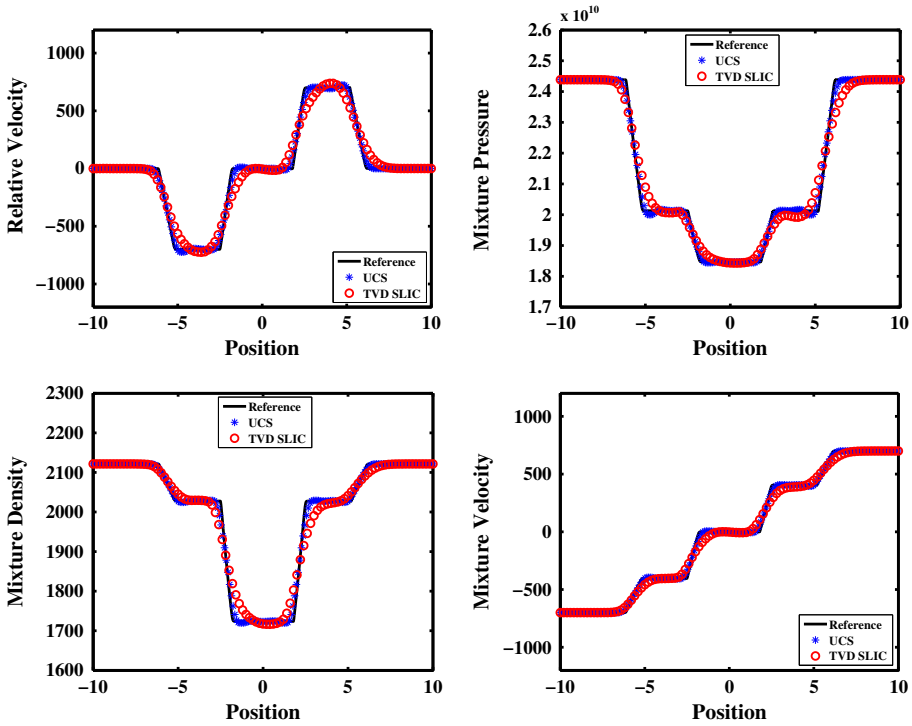

Figure 3. Comparison of calculated results for test case 4.4 at time $t = 0.0008$. The symbols represent two different numerical methods, namely, the TVD SLIC scheme and the UCS approach of [41]. The solid line corresponds to the reference solution provided on a very fine mesh of 6000 using the TVD SLIC scheme. A CFL of 0.9 is employed within the TVD SLIC scheme, whereas 0.485 for the UCS. As in Figures 1 and 2, plots display the relative velocity (m s^{-1}) and mixture pressure (Pa) from top left to right and mixture density (kg m^{-3}) and mixture velocity (m s^{-1}) from bottom left to right. Comparisons of coarse mesh results for both methods validate the model equations for the conducted Riemann problem.

As a further validation and comparison, we display in Figure 3 simulation results using an independent numerical method, namely, the UCS [41]. Further, the UCS and TVD SLIC methods are employed to provide such results at time $t = 0.0008$ on a mesh of 100 cells. It is easy to note that both methods reproduce the same wave structure as the reference solutions. Further, an excellent agreement between the TVD SLIC and UCS methods and the reference solutions are clearly observed. The quality of the results obtained by the TVD SLIC scheme is much better than the UCS. This is clearly observed by the overshoots and undershoots after the rarefaction waves and across the repeated contact discontinuity. Finally, we may conclude that system (13) renders the current severe test case correctly, and the present TVD SLIC scheme can capture expansion tube problems within volcanic processes accurately.

4.2. Mixture shock tube problem

In this test case, the magma and gas are under high velocities on the left of the tube and with low velocities on the right of the tube. Further, the following Riemann data are considered

- Magma

$$(\rho_1, u_1, s_1)_L = (2500.0 \text{ kg/m}^3, 1000.0 \text{ m/s}, 7556.5895 \text{ J/K kg}),$$
$$(\rho_1, u_1, s_1)_R = (1800.0 \text{ kg/m}^3, 400.0 \text{ m/s}, 7556.5895 \text{ J/K kg}).$$

- Gas

$$(\alpha, \rho_2, u_2, s_2)_L = (0.6, 1977.0 \text{ kg/m}^3, 700.0 \text{ m/s}, 12658.879 \text{ J/K kg}),$$
$$(\alpha, \rho_2, u_2, s_2)_R = (0.6, 1000.0 \text{ kg/m}^3, 100.0 \text{ m/s}, 12658.879 \text{ J/K kg}),$$

DOI: 10.1002/fld

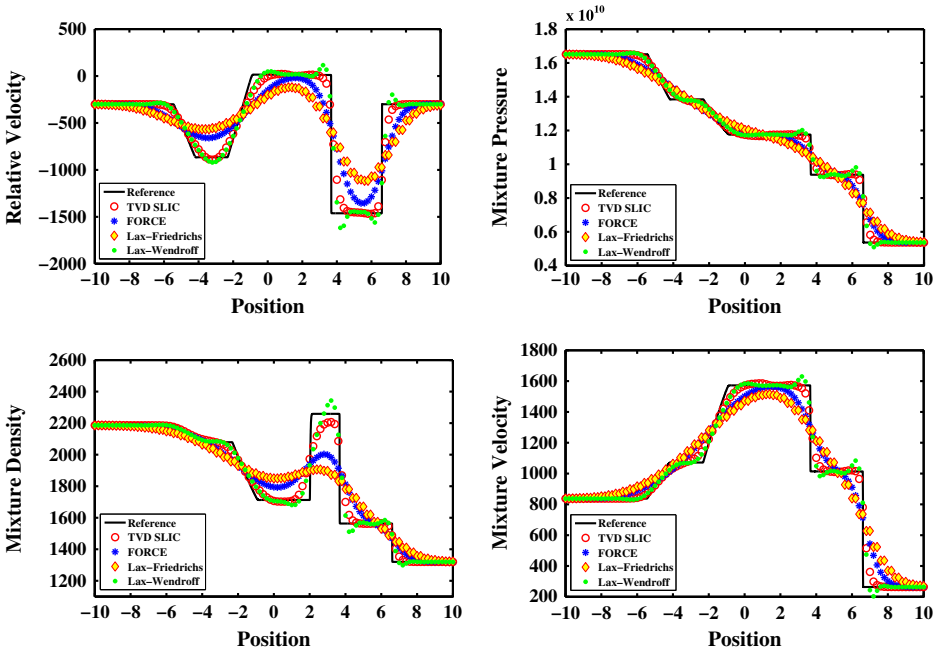

Figure 4. Solution of the mixture shock tube problem for test case 4.2 calculated on a coarse mesh with 100 cells at time $t = 0.0013$. The computed results are the symbols and the solid lines represent the reference solution, which is provided by the TVD SLIC scheme with the SUPERBEE limiter on a very fine mesh of 6000. Each plot shows four different results for different numerical methods, namely, the TVD SLIC, FORCE, Lax–Friedrichs, and Lax–Wendroff methods, respectively. $CFL = 0.9$. The top left and right panels show the relative velocity (m s^{-1}) and mixture pressure (Pa), whereas the bottom left and right panels illustrate the mixture density (kg m^{-3}) and mixture velocity (m s^{-1}). The results are similar to the reference solutions; however, difference between them is clearly observed within the resolution of the repeated contact wave.

for which the Riemann reference solution structure is composed of two left-traveling rarefaction waves associated with λ_1 and λ_2, which are followed by a repeated contact waves for the mixture and then two right-traveling shock waves associated with the eigenvalues λ_5 and λ_6, respectively. Numerical results of the main flow variables for the reference solution (solid lines), first-order and second-order methods (symbols) are displayed in Figure 4.

In Figure 4, the approximate solutions (symbols) are computed with the TVD SLIC, FORCE, Lax–Friedrichs, and Lax–Wendroff methods on a coarse mesh of 100 cells at the time $t = 0.0013$. The results are also compared with the reference solution reproduced on a very fine mesh of 6000 cells using the TVD SLIC scheme. As one can see from the comparisons, the four methods recover the same wave structure as the reference solutions for this coarse mesh performance. However, the four methods differ in their ability to capture discontinuities and wave structures as illustrated in Figure 4. The results obtained with the Lax–Friedrichs scheme are paired, which is an identical property of producing coarse mesh results. It could be noticed also that the results provided by the Lax–Wendroff scheme exhibit undershoot and overshoot through all the sharp discontinuities. The simulation results with the TVD SLIC scheme captures the middle weaves more sharply and accurately without spurious oscillations for this considered Riemann data. Additionally, the head and tail of the left-traveling rarefaction waves accurately recovered as sharp features with the TVD SLIC scheme. The results provided by the TVD SLIC scheme on a coarse mesh for the mixture and relative velocity profiles plotted in Figure 4 show numerical dissipation across the middle wave. This is due to the nonlinearity of the model equations and to the given Riemann initial conditions. With further increase in the number of computational cells, however, the reduction of these numerical dissipation is achieved as observed in Figure 5. This is clearly figured out through the various mesh

DOI: 10.1002/fld

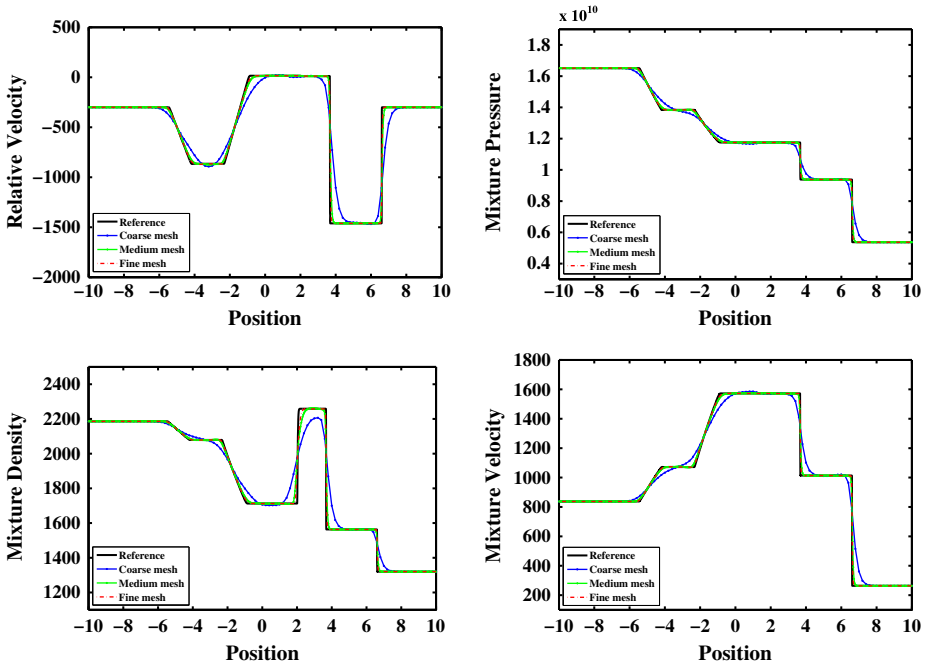

Figure 5. Mesh convergence study for the mixture shock tube problem 4.2 at time $t = 0.0013$. The results are computed on coarse, medium, and fine meshes, respectively. With increasingly finer mesh resolution for the TVD SLIC scheme, the results are qualitatively very similar to the standard reference solutions, and numerical dissipation is reduced. The reference solution (solid lines) is obtained using the TVD SLIC scheme. On the top: plots for the relative velocity (m s^{-1}) and mixture pressure (Pa). On the bottom: mixture density (kg m^{-3}) and mixture velocity (m s^{-1}).

resolutions displayed in Figure 5. This figure also illustrates that the TVD SLIC scheme can capture complete wave structure correctly with gradually refined mesh.

Figure 6 shows a comparison of simulation results from the TVD SLIC and UCS methods (symbols) with the reference solutions (solid lines). Numerical results are carried out using a mesh of 100 cells at the time $t = 0.0013$. In these results, the wave structure is well predicted by both methods. The mixture velocity and relative velocity profiles clearly show numerical dissipation across the middle wave. However, one can note that the TVD SLIC scheme gives better resolution for the current wave structure than the UCS. The overall result is that both methods are in a very good agreement with the reference solutions for all profiles.

4.3. Gas–magma mixture collision

The final test case concerns the simulation of the Riemann gas–magma mixture collision with the following Riemann problem

- Magma

$$(\rho_1, u_1, s_1)_L = (2500.0\ \text{kg/m}^3,\quad 1000.0\ \text{m/s},\ 7556.5895\ \text{J/K kg}),$$
$$(\rho_1, u_1, s_1)_R = (2500.0\ \text{kg/m}^3, -1000.0\ \text{m/s},\ 7556.5895\ \text{J/K kg}).$$

- Gas

$$(\alpha, \rho_2, u_2, s_2)_L = (0.8, 1562.0\ \text{kg/m}^3,\quad 400.0\ \text{m/s},\ 12658.879\ \text{J/K kg}),$$
$$(\alpha, \rho_2, u_2, s_2)_R = (0.8, 1562.0\ \text{kg/m}^3, -400.0\ \text{m/s},\ 12658.879\ \text{J/K kg}).$$

The solution of this problem consists of two left and two right shock waves separated by a multiple contact discontinuity. Solutions to this Riemann problem are calculated at time $t = 0.0009$. An

DOI: 10.1002/fld

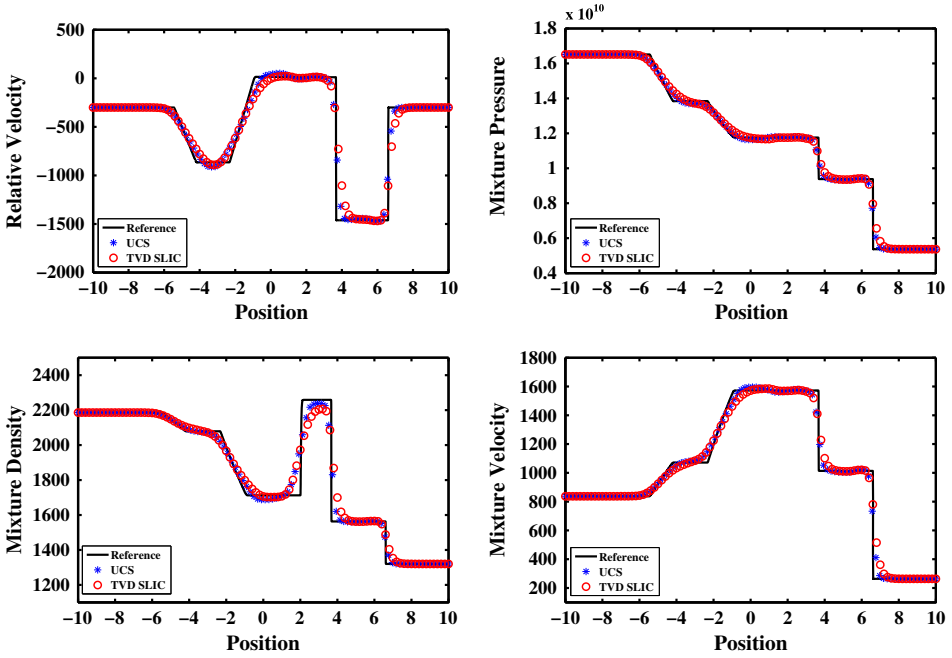

Figure 6. Mixture shock tube problem 4.2. Comparison of calculated results with the UCS approach and the TVD SLIC scheme at time $t = 0.0013$ with 100 mesh cells. The symbols indicate such methods, whereas the solid line corresponds to the reference solutions. $CFL = 0.9$ is used for the TVD SLIC scheme and 0.485 within the UCS approach. The top left and right panels show the relative velocity (m s^{-1}) and mixture pressure (Pa), respectively. Whereas the bottom left and right panels the mixture density (kg m^{-3}) and mixture velocity (m s^{-1}), respectively. Comparisons of both methods show notable differences in the behavior.

accurate reference solution is generated using the TVD SLIC scheme. Results for this test case are displayed in Figures 7 and 8, respectively. Figure 7 presents numerical results with a coarse mesh of 100 cells. These results are obtained with the four different numerical methods (symbols) and compared with the reference solutions (solid lines). As one can observe from this figure, strong waves are propagated in opposite directions. This is due to magma fragmentation into ash that is caused by the effect of high gas volume fraction where the relative velocity between gas and magma becomes significant. When these effects are taken into account, collision induces large pressure variations as illustrated in Figures 7 and 8. The numerical results are in excellent agreement with reference solutions. Further, the TVD SLIC scheme is capable of resolving shock waves propagation and oscillation-free profiles at sharp discontinuities for the current Riemann problem. As in the previous test cases, the results of Lax–Friedrichs scheme are paired as usual, whereas the results of Lax–Wendroff scheme suffer undershoot and overshoot through all the sharp discontinuities.

In Figure 8, the results from the UCS scheme of [41] are compared with those from the TVD SLIC scheme. Both numerical results (red and blue symbols) are compared with the reference solutions (solid lines) and show very good agreement with these reference solutions even in a coarse mesh. In particular, sharpness of the full wave structure, associated with the genuinely nonlinear and linearly degenerate fields, is clearly observed using the TVD SLIC scheme. We also note that the results provided by the TVD SLIC scheme are better than the results of the UCS scheme. From the comparison made in this figure, one may conclude that both numerical methods and model equations perform very well on this Riemann problem of volcanic eruptions.

We end this test case by a two-dimensional version of the current Riemann problem. Within a computational context, we choose to simulate this test case using the UCS scheme of [41] on a computational domain $[-10, 10] \times [-10, 10]$. The simulation results are displayed in Figure 9. In these simulation results, the mesh contains 100×100 cells together with $CFL = 0.485$ at the time $t = 0.0009$. The provided resolutions are able to capture the expected wave behavior of gas and

DOI: 10.1002/fld

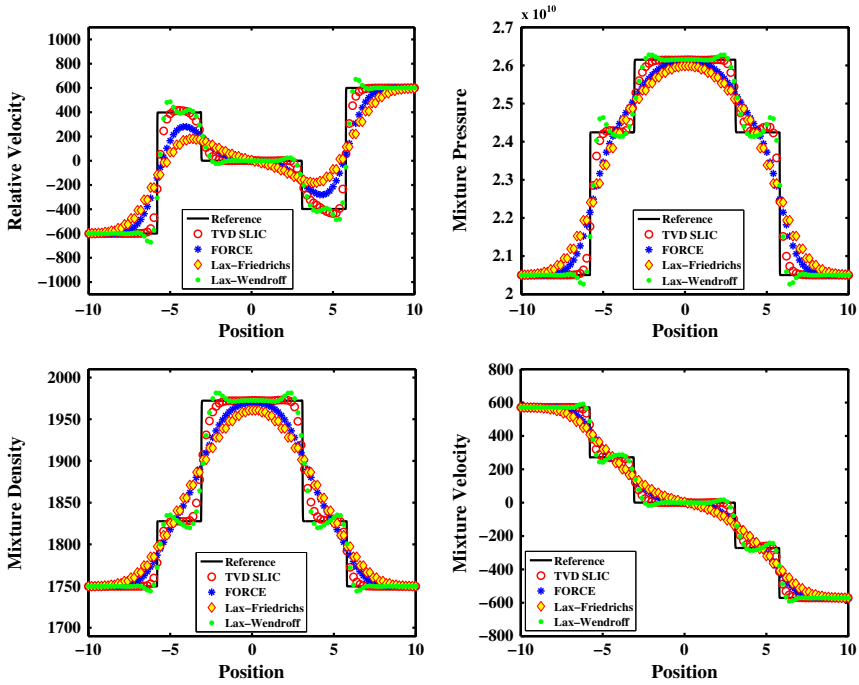

Figure 7. Simulation results of gas–magma mixture collision (test case 4.3). Representation of the relative velocity (m s^{-1}), mixture pressure (Pa), top panels and mixture density (kg m^{-3}) and mixture velocity (m s^{-1}), bottom panels, with 100 mesh cells at time $t = 0.0009$. The symbols indicate the values of the four numerical methods, whereas the solid lines represent the reference solution, which is provided on a very fine mesh using the TVD SLIC scheme. The wave structure is similar for all methods.

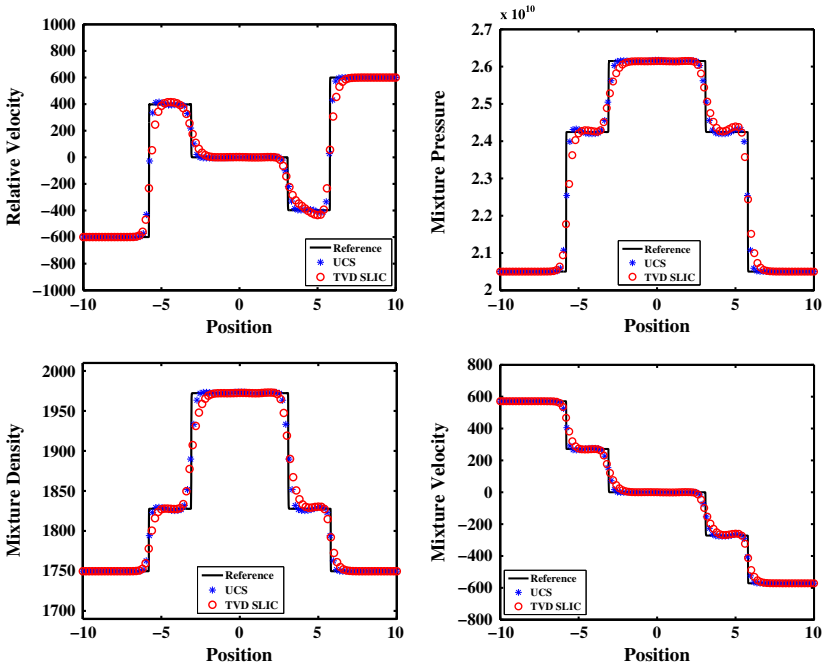

Figure 8. Comparison between the TVD SLIC scheme and UCS approach for gas–magma mixture collision (test case 4.3) at time $t = 0.0009$. $CFL = 0.485$ has been used for the UCS approach. The top left and right panels show the relative velocity (m s^{-1}) and mixture pressure (Pa), respectively, whereas the bottom left and right panels display the mixture density (kg m^{-3}) and mixture velocity (m s^{-1}), respectively. The solid line corresponds to the TVD SLIC scheme on a very fine mesh.

DOI: 10.1002/fld

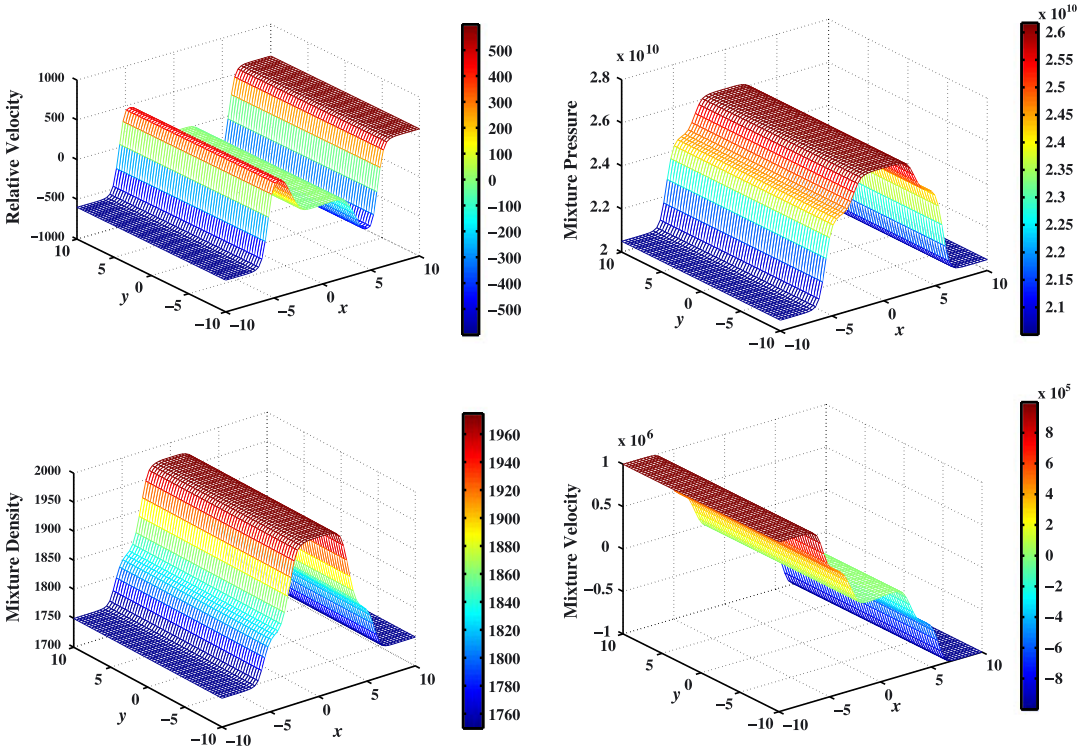

Figure 9. Profiles of the 2D gas–magma mixture collision (test case 4.3). The upper panels show the relative velocity (m s^{-1}) and mixture pressure (Pa), respectively, whereas the lower panels show the mixture density (kg m^{-3}) and mixture velocity (m s^{-1}), respectively. The computations correspond to a coarse mesh of 100×100 cells at time $t = 0.0009$. Simulations are carried out by the UCS together with CFL number of 0.485.

magma mixture collision. It can be noticed that the displayed results are well simulated and free from any numerical dissipation.

4.4. Influence of the drag force

The application and influence of the interphase drag source term, π, appearing in the relative velocity Equation 6 is investigated. This is shown within the context of gas–magma mixture collision test case 4.3. Because of magma fragmentation, the following drag function, κ, is found to fulfill the purpose of the current paper

$$\kappa = \frac{3}{8}\frac{C_D}{r_b}\rho c(1-\alpha)|u_r|, \tag{30}$$

which is similar to that used in most of the existing drag functions and in agreement with the general structure proposed in the literature. See for example [16, 36, 37, 42] and the references therein. Here, C_D is the drag coefficient and r_b is the radius of the fragmented magma particles. The drag force (12), therefore, can be written as

$$\pi = \frac{3}{8}\frac{C_D}{r_b}\rho c(1-\alpha)u_r|u_r|. \tag{31}$$

It is clear that the aforementioned drag force depends on both the radius of the fragmented magma particles and on the drag coefficient along with other flow properties. Because the gas volume fraction is considered sufficiently large, 0.8, and the relative motion is taken into account between the magma fragments and gas, fragmentation produces a wide range of magma particle sizes along

DOI: 10.1002/fld

with interfacial drag efforts. This mainly depends on both the eruption styles and geophysical properties of the two phase systems. Because this study is devoted to compressible gas and magma flows, we adopted different values for both the drag coefficient and the radius of magma particles as we shall see later.

To continue, Figures 10–13 show a comparison between the source and no source terms of the current model equations. The source terms results are obtained through time splitting approach using the TVD SLIC scheme with a reduced CFL number from 0.9 to 0.01 and with a coarse mesh of 100 cells at the time $t = 0.0009$. Figure 10 illustrates the simulation results of the relative velocity, mixture pressure, mixture density, and mixture velocity for different drag coefficient values ($C_D = 0.001, 0.1, 1.0, 100.0, 1000.0$) and for fixed radius, r_b, of 9.33 μm [43]. These values exploit the fact that both phases are given high densities and velocities along with large gas fraction where fragmentation occurs as shown in test case 4.3. It is worth to note that the results do not show any significant change, and the behavior is basically the same after $C_D = 1000.0$. One can observe from Figure 10 that increasing the value C_D leads to an enlargement of the solution smearing zone. It is also notable that with an increased C_D, the two phases have the same velocity, see the relative velocity profile of Figure 10. That is, the current model approaches the velocity equilibrium case as it happens during volcanic processes. In Figure 11, a comparison of the relative velocity calculated by the present model equations with and without the drag coefficient source term for a fixed radius is illustrated. Both curves are produced on a very fine mesh of 6000 at the time $t = 0.0009$. It is noted that both phases have the same velocity regardless if the mesh cell is coarse or fine.

Next, we investigate the effect of the radius, r_b, for fixed drag coefficient C_D. We have chosen $C_D = 1$ and simulated gas–magma mixture collision for $r_b = 0.05, 0.01, 1.0, 6.2, 9.33$ μm. The results are plotted in Figure 12 for the same flow variables as in Figure 10. These plots clearly show

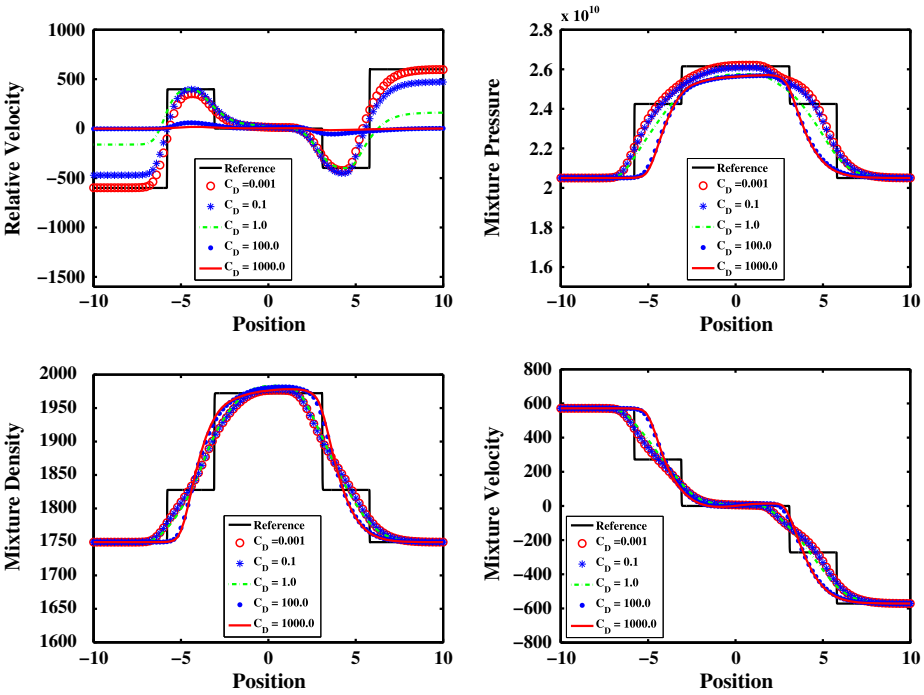

Figure 10. Influence of the value of C_D on the solution of gas–magma mixture collision (test case 4.3). Solutions provided using the TVD SLIC scheme with a coarse mesh of 100 cells at time $t = 0.0009$. Different runs are carried out to a CFL of 0.01 with C_D varying from the lowest possible value of 0.001 to the highest possible value of 1000.0. The patterns are similar to that of Figures 7 and 8. Top panels: relative velocity (m s^{-1}) and mixture pressure (Pa), respectively. Bottom panels: mixture density (kg m^{-3}) and mixture velocity (m s^{-1}), respectively. The solid lines indicate the reference solutions provided on a very fine mesh using the TVD SLIC scheme, whereas the symbols correspond to the drag coefficient C_D.

DOI: 10.1002/fld

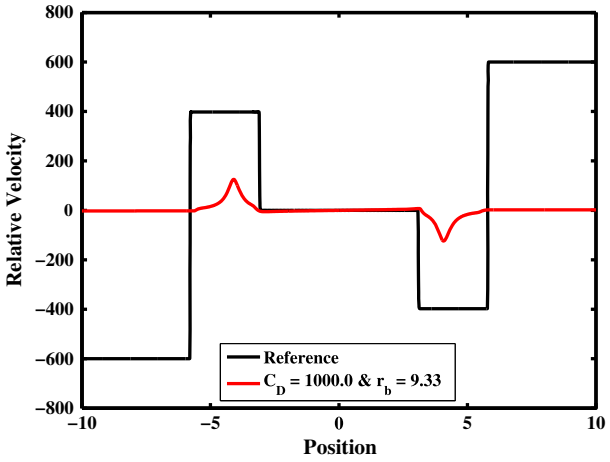

Figure 11. Effect of the highest possible value of C_D and r_b on the solution of gas–magma mixture collision of Figure 10. Resolution for the relative velocity on a very fine mesh of 6000 using the TVD SLIC scheme at time $t = 0.0009$.

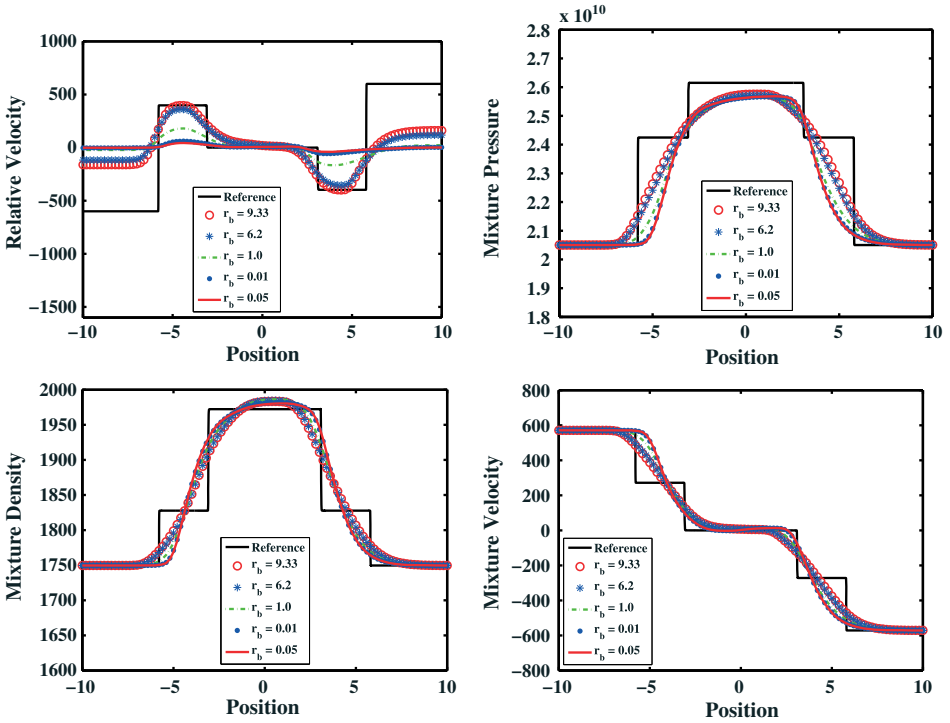

Figure 12. Influence of the radius r_b on the solution of gas–magma mixture collision (test case 4.3). As in Figure 10, solutions are obtained by using the TVD SLIC scheme with a coarse mesh of 100 cells at time $t = 0.0009$ and a CFL value of 0.01. The results are carried out with $C_D = 1.0$ and varying radius r_b from the lowest possible value of 0.05 μm to the highest possible value of 9.33 μm. The top left and right panels display the relative velocity (m s^{-1}) and mixture pressure (Pa), respectively. The mixture density (kg m^{-3}) and mixture velocity (m s^{-1}) are shown in the bottom left and right panels, respectively. The solid lines indicate the reference solutions provided on a very fine mesh using the TVD SLIC scheme, whereas the symbols correspond to the radius r_b of the fragmented magma particles.

DOI: 10.1002/fld

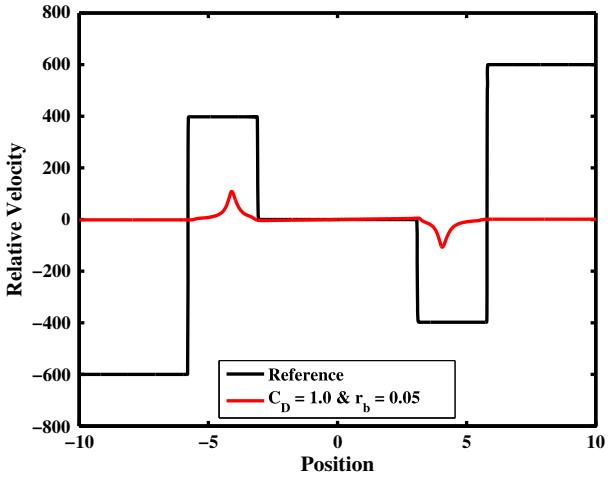

Figure 13. Effect of the lowest possible radius r_b, 0.05 μm, with a C_D of 1.0 on the solution of gas–magma mixture collision of Figure 10. Resolution for the relative velocity on a very fine mesh of 6000 using the TVD SLIC scheme at time $t = 0.0009$.

the influence of different values of the fragmented magma particles radius on the complete wave structures. There are discrepancies for the mixture pressure, mixture density, and mixture velocity across the middle wave in comparison with the reference solution of the same plots of Figure 10. However, it is clear that there is an appreciable difference in both profiles of the relative velocity, see Figures 10 and 12. In particular, the relative velocity profiles are extrapolated at the boundaries but have the same behavior across the middle wave. Figure 13 displays the computed relative velocity and compares the reference solution with the fragmented magma particles radius source term for a fixed drag coefficient. Both curves are produced on a very fine mesh of 6000 at time $t = 0.0009$. As evident in Figures 12 and 13, the current model approaches the velocity equilibrium with decreased fragmented magma particles radius. The results with decreased fragmented magma particle radius do not show any significant change, and the behavior is basically the same after $r_b = 0.05$ μm. Despite our choice of the interphase drag source term, however, the two phases have the same velocity with increased drag coefficient and decreased fragmented magma particles radius.

5. CONCLUSION AND FUTURE WORK

This paper provides validation arguments to a thermodynamically mathematical model for gas–magma mixtures in which fragmentation is taking place. The model has several features not shared with other models of volcanic processes. Mostly, it accounts explicitly for fully unsteady and non-equilibrium processes, phase constituents and prevents the need to specify specific physical assumptions such as velocity equilibrium between phases. Instead, the effect of the relative motion between phases evolves as a consequence of a differential equation. The mathematical model also includes other features not present in competing models such as the fully hyperbolic and fully conservative nature of the governing equations. On such basis, the model can accommodate any numerical method of interest.

Based on the Riemann problem, the application of the Godunov methods of centered-type to the model equations has been performed directly. The model has been successfully simulated with the numerical test cases presented in this paper, although we did not try to simulate a specific eruption. As such, these test cases are conducted under conditions that are typical for highly explosive eruptions. It is shown that the model equations are able to predict relatively high phase initial data of both gas and magma phases. Further, the model appeared to perform well with such data producing results free from spurious oscillation phenomena. These results show qualitative and quantitative agreement with other methods available in the literature. The simulations, therefore, are able to

DOI: 10.1002/fld

demonstrate as a novel platform to provide new insights into volcanic phenomena with unsteady velocity non-equilibrium.

The existence of such features of the current work offers a new opportunity to explore various aspects of volcanic processes using the proposed model equations. Further investigation of the model would clarify the velocity non-equilibrium of various volcanic eruption styles and regimes. Extensive simulations in multidimensional space are planned for the future where comparisons with field observations and laboratory experiments are possible. This may provide a starting point for analyzing the relative velocity within volcanic processes and will motivate other researchers in the field.

ACKNOWLEDGEMENTS

A short version of this paper was presented at the 8th Symposium on Numerical Analysis of Fluid and Flow and Heat Transfer-Numerical Fluids Symposium 2013 held in Rhodes, Greece, 21st–27th, September 2013. The author would like to acknowledge the stimulating discussions of volcanic eruptions with M. de' Michieli Vitturi of Istituto Nazionale di Geofisica e Vulcanologia (INGV), Sezione di Pisa, Pisa, Italy, where this work was initiated during the author's stay in 2012 at the Mathematics Section, Abdus Salam International Centre for Theoretical Physics (ICTP), Trieste, Italy. The authors gratefully acknowledge support from the German Jordanian University.

REFERENCES

1. Carcano S, Bonaventura L, Esposti Ongaro T, Neri A. A semi-implicit, second-order-accurate numerical model for multiphase underexpanded volcanic jets. *Geoscientific Model Development Discussion* 2013; **6**:399–452.
2. Bercovici D, Michaut C. Two-phase dynamics of volcanic eruptions: compaction, compression and the conditions for choking. *Geophysical Journal International* 2010; **182**:843–864.
3. Marcia P, LeVeque RJ. High-resolution finite volume methods for dusty gas jets and plumes. *SIAM: SIAM Journal on Scientific Computing* 2006; **28**:1335–1360.
4. Ishii M, Hibiki T. *Thermo-fluid Dynamics of Two-Phase Flow* (2nd edn). Springer: New York, 2011.
5. Städtke H. *Gasdynamic Aspects of Two-Phase Flow: Hyperbolicity, Wave Propagation Phenomena, and Related Numerical Methods* (1st edn). Wiley-VCH: Weinheim, 2006.
6. Romensky EI. Hyperbolic systems of thermodynamically compatible conservation laws in continuum mechanics. *Mathematical and Computer Modelling* 1998; **28**:115–130.
7. Resnyanskya AD, Bourne NK. Shock-wave compression of a porous material. *Journal of Applied Physics* 2004; **95**:1760–1769.
8. Romenski E, Drikakis D, Toro E. Conservative models and numerical methods for compressible two-phase flow. *Journal of Scientific Computing* 2010; **42**:68–95.
9. La Spina G, de' Michieli Vitturi M. High-resolution finite volume central schemes for a compressible two-phase model. *SIAM: SIAM Journal on Scientific Computing* 2012; **34**:B861–B880.
10. Zeidan D, Touma R. On the computations of gas-solid mixture two-phase flow. *Advances in Applied Mathematics and Mechanics* 2014; **6**:49–74.
11. Godunov SK, Romenski E. *Elements of Continuum Mechanics and Conservation Laws*. Kluwer Academic/Plenum Publishers: New York, 2003.
12. Textor C, Graf H, Longo A, Neri A, Ongaro TE, Papale P, Timmreck C, Ernst GGJ. Numerical simulation of explosive volcanic eruptions from the conduit flow to global atmospheric scales. *Annals of Geophysics* 2005; **48**: 817–842.
13. Koyaguchi T, Mitani NK. A theoretical model for fragmentation of viscous bubbly magmas in shock tubes. *Journal of Geophysical Research* 2005; **110**:B10202.1–B10202.21.
14. Koyaguchi T, Mitani NK. The fluid mechanics inside a volcano. *Annual Review of Fluid Mechanics* 2007; **39**: 321–356.
15. Slezin YB. The mechanism of volcanic eruptions (a steady state approach). *Journal of Volcanology and Geothermal Research* 2003; **122**:7–50.
16. Neri A, Ongaro TE, Macedonio G, Gidaspow D. Multiparticle simulation of collapsing volcanic columns and pyroclastic flow. *Journal of Geophysical Research* 2003; **108**:B4 2202–B4 2224.
17. Melnik O, Barmin AA, Sparks RSJ. Dynamics of magma flow inside volcanic conduits with bubble overpressure buildup and gas loss through permeable magma. *Journal of Volcanology and Geothermal Research* 2005; **143**:53–68.
18. Koyaguchi T, Scheu B, Mitani MK, Melnik O. A fragmentation criterion for highly viscous bubbly magmas estimated from shock tube experiments. *Geophysical Journal of the Royal Astronomical Society* 1976; **45**:543–556.
19. Wilson L. Explosive volcanic eruptions-III. Plinian eruption columns. *Journal of Volcanology and Geothermal Research* 2008; **178**:58–71.
20. Prandtl L. *The Elements of Fluid Mechanics*. Blackie: London, 1954.
21. Kieffer SW, Sturtevant B. Laboratory studies of volcanic jets. *Journal of Geophysical Research* 1984; **89**:8253–8268.

DOI: 10.1002/fld

22. Turcotte DL, Ockendon H, Ockendon JR, Cowley SJ. A mathematical model of vulcanian eruptions. *Geophysical Journal Znt* 1990; **103**:211–217.
23. Woods AW. The fluid dynamics and thermodynamics of eruption columns. *Bull. Volcanol.* 1988; **50**:169–193.
24. Valentine GA, Wohletz KH. Numerical models of Plinian eruption columns and pyroclastic flows. *Journal of Geophysical Research* 1989; **94**:1867–1887.
25. Kozono T, Koyaguchi T. Effects of relative motion between gas and liquid on 1-dimensional steady flow in silicic volcanic conduits: 1. An analytical method. *Journal of Volcanology and Geothermal Research* 2009; **180**:21–36.
26. Kozono T, Koyaguchi T. Effects of relative motion between gas and liquid on 1-dimensional steady flow in silicic volcanic conduits: 2. Origin of diversity of eruption styles. *Journal of Volcanology and Geothermal Research* 2009; **180**:37–49.
27. Ramos JI. One-dimensional, time-dependent, homogeneous, two-phase flow in volcanic conduits. *International Journal for Numerical Methods in Fluids* 1995; **21**:253–278.
28. Ramos JI. Two-dimensional simulations of magma ascent in volcanic conduits. *International Journal for Numerical Methods in Fluids* 1999; **29**:765–789.
29. Zeidan D, Romenski E, Slaouti A, Toro EF. Numerical study of wave propagation in compressible two-phase flow. *International Journal for Numerical Methods in Fluids* 2007; **54**:393–417.
30. Toro E, Billett S. Centred TVD schemes for hyperbolic conservation laws. *IMA Journal of Numerical Analysis* 2000; **20**:47–79.
31. Thevand N, Daniel E, Loraud JC. On high-resolution schemes for solving unsteady compressible two-phase dilute viscous flows. *International Journal for Numerical Methods in Fluids* 1999; **31**:681–702.
32. Toro EF. *Riemann Solvers and Numerical Methods for Fluid Dynamics: A Practical Introduction* (3rd edn). Springer: Berlin Heidelberg, 2009.
33. Wilson L. Explosive volcanic eruptions-II the atmospheric trajectories of pyroclasts. *Geophysical Journal of the Royal Astronomical Society* 1972; **30**:381–392.
34. Bower SM, Woods AW. On the dispersal of clasts from volcanic craters during small explosive eruptions. *Journal of Volcanology and Geothermal Research* 1996; **73**:19–32.
35. Enwald H, Peirano E, Almstedt AE. Eulerian two-phase flow theory applied to fluidization. *International Journal of Multiphase Flow* 1996; **22**:21–66.
36. Yoshida S, Koyaguchi T. A new regime of volcanic eruption due to the relative motion between liquid and gas. *Journal of Volcanology and Geothermal Research* 1999; **89**:303–315.
37. de' Michieli Vitturi M, Neri A, Esposti Ongaro T, Lo Savio S, Boschi E. Lagrangian modeling of large volcanic particles: application to Vulcanian explosions. *Journal of Geophysical Research* 2010; **115**:B8:8206–18.
38. Thompson PA. *Compressible Fluid Dynamics (Advanced Engineering Series)*. McGraw-Hill Inc.: US, 1972.
39. Mader C. *Numerical Modeling of Detonations*. University of California Press Ltd. London: England, 1979.
40. Zeidan D, Touma R, Slaouti A. Using gas–solid mixture conservation laws for volcanic eruptions. *AIP Conference Proceedings* 1558:180–183.
41. Touma R. Central unstaggered finite volume schemes for hyperbolic systems: applications to unsteady shallow water equations. *Applied Mathematics and Computation* 47–59; **213**.
42. Degruyter W, Bachmann O, Burgisser A, Manga M. The effects of outgassing on the transition between effusive and explosive silicic eruptions. *Earth and Planetary Science Letters* 2012; **349**:161–170.
43. Niemeier U, Timmreck C, Graf HF, Kinne S, Rast S, Self S. Initial fate of fine ash and sulfur from large volcanic eruptions. *Atmospheric Chemistry and Physics* 2009; **9**:9043–9057.

DOI: 10.1002/fld